

# Robust and Efficient Segmentation of Cross-domain Medical Images

Xingqun Qi, Zhuojie Wu, Min Ren, Muiyi Sun, and Zhenan Sun, *Senior Member, IEEE*

**Abstract**—Efficient medical image segmentation aims to provide accurate pixel-wise prediction for the medical images with the lightweight implementation framework. However, lightweight frameworks generally fail to achieve high performance, and suffer from the poor generalizable ability on cross-domain tasks. In this paper, we propose a generalizable knowledge distillation method for robust and efficient segmentation of cross-domain medical images. Primarily, we propose the Model-Specific Alignment Networks (MSAN) to provide the domain-invariant representations which are regularized by a Pre-trained Semantic AutoEncoder (P-SAE). Meanwhile, a customized Alignment Consistency Training (ACT) strategy is designed to promote the MSAN training. With the domain-invariant representative vectors in MSAN, we propose two generalizable knowledge distillation schemes, Dual Contrastive Graph Distillation (DCGD) and Domain-Invariant Cross Distillation (DICD). Specifically, in DCGD, two types of implicit contrastive graphs are designed to represent the intra-coupling and inter-coupling semantic correlations from the perspective of data distribution. In DICD, the domain-invariant semantic vectors from the two models (*i.e.*, teacher and student) are leveraged to cross-reconstruct features by the header exchange of MSAN, which achieves generalizable improvement for both the encoder and decoder in the student model. Furthermore, a metric named Fréchet Semantic Distance (FSD) is tailored to verify the effectiveness of the regularized domain-invariant features. Extensive experiments conducted on the Liver and Retinal Vessel Segmentation datasets demonstrate the priority of our method, in terms of performance and generalization on lightweight frameworks.

**Index Terms**—Medical Image Segmentation, Knowledge Distillation, Model Generalization, Contrastive Graph

## I. INTRODUCTION

MEDICAL image segmentation (MIS) refers to obtaining the accurate pixel-level semantic interpretation on clinical medical images. With its significant practical values for auxiliary diagnosis, MIS has drawn impressive progress with the development of deep neural networks [1]–[3]. Numerous works have emerged and demonstrated superior performances, even in complex scenarios (*i.e.* cross-domain medical image segmentation) [4]–[9]. However, these models heavily rely on massive parameters and deeper network frameworks, which

Xingqun Qi is an intern at the Center for Research on Intelligent Perception and Computing, National Laboratory of Pattern Recognition, Institute of Automation, Chinese Academy of Sciences, Beijing, China, 100190, (e-mail: xingqunqi@gmail.com).

Zhuojie Wu is with the School of Artificial Intelligence / Automation, Beijing University of Posts and Telecommunications, Beijing, China, 100876, (e-mail: zhuojiewu@bupt.edu.cn).

Min Ren, Muiyi Sun and Zhenan Sun are with the Center for Research on Intelligent Perception and Computing, National Laboratory of Pattern Recognition, Institute of Automation, Chinese Academy of Sciences, Beijing, China, 100190, (e-mails: min.ren@cripac.ia.ac.cn; muiyi.sun@cripac.ia.ac.cn; znsun@nlpr.ia.ac.cn). (Corresponding author: Muiyi Sun)

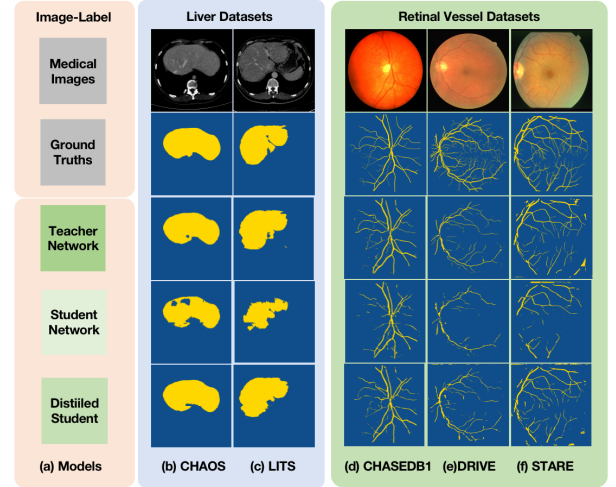


Fig. 1. Liver and vessel segmentation results on cross-domain datasets of scratch-trained teacher, scratch-trained student and the distilled student by our method. For each multi-domain data group, there are input images, ground truths and predictions of these three networks (from top row to the bottom). Segmented foreground pixels are colored in yellow. We test these samples on the liver datasets with the pre-trained model on CHAOS training set, and test the samples on vessel datasets with the pre-trained model on CHASEDB1 training set. Our generalizable knowledge distillation framework could improve the performance and generalizable ability of the student networks jointly. The results on LITS, DRIVE, and STRAE datasets show the generalization superiority of our method. Zoom in for better details.

could not be applied on edge or embedded devices. Meanwhile, due to the high-resolution popularity of most medical images (*i.e.*  $10^5 \times 10^5$  in [33]), shallow models are not sufficient to learn their rich spatial contextual information. Obtaining high-accuracy segmentation from the medical images with lightweight models still remains challenging, especially in complex (*i.e.* cross-domain) scenarios. To address this issue, various lightweight technologies are taken into consideration for efficient medical image segmentation [10], [11]. In recent years, efficient medical image segmentation attracts plentiful attention since its great practical value for medical image analysis in real scenes.

Lightweight technologies can be roughly divided into compression-based approaches [12]–[14], pruning-based approaches [15]–[17], and knowledge distillation-based ones [18]–[22]. Recently, knowledge distillation-based approaches show better potential for the efficient medical image segmentation tasks comparing with the previous two types. Benefiting from the semantic information distilled from the powerful complex networks (called teacher), the lightweight

models (called student) achieve significant performance improvement in single-domain tasks. However, the vast majority of these methods [23]–[25] ignore the poor performances of lightweight models on cross-domain datasets, even for the same semantic-class tasks as depicted in Fig. 1. Generally, the complicated models have better domain-invariant representation capabilities which are not be potentially explored by previous knowledge distillation methods. Therefore, it is worth exploring the high-performance knowledge distillation approaches with a more robust and generalizable manner.

Transferring the domain-invariant features provides a good paradigm for the lightweight models to improve their generalizable abilities [26]–[28]. Among the approaches to extract the domain-invariant knowledge, contrastive learning based methods have illustrated superiority, due to the fully utilization of enormous augmented data [29]–[31] through an unsupervised way. Therefore, in this paper, we intend to explore the generalizable knowledge by establishing contrastive correlations between the source images and their augmented samples. However, as for semantic segmentation tasks, it is difficult to explicitly construct the pixel-wise contrastive supervision templates. Thus, we leverage two types of implicit contrastive graphs to represent the semantic domain-shift between different augmented samples. Different from the previous works [32], [33], the graphs involved in our framework provide more accessible implicit associations from teacher to student.

Motivated by the above observations, we design a generalizable knowledge distillation framework (dubbed as GKD) for robust and efficient cross-domain medical image segmentation. The proposed GKD mainly consists of the Model-Specific Alignment Networks (MSAN), a Dual Contrastive Graph Distillation (DCGD) schema, and a Domain-Invariant Cross Distillation (DICD) schema as illustrated in Fig. 2.

The GKD framework can be treated as generalizable knowledge transfer from the teacher to student models, leading to the mapping from the domain-specific medical images to the domain-invariant dense predictions. In order to obtain consistent semantic representations from the teacher and student networks, we design the MSAN with the Alignment Consistency Training (ACT) strategy. More specifically, we firstly introduce a Pre-trained Semantic AutoEncoder (P-SAE) for obtaining the domain-invariant semantic representations. Then, the teacher and student networks are scratch-trained by simple task-driven supervision. Afterward, we construct the MSAN for extracting semantic vectors from the teacher and student models, respectively. The paired image and label are separately fed into the pre-trained teacher (or student) and the above-mentioned P-SAE. We enforce the vectors extracted by MSAN to align with the semantic representative vectors from P-SAE. In this way, the Student Alignment Network (SAN) receives consistent regularization with the Teacher Alignment Network (TAN), which contributes to the emergence of the domain-invariant semantic latent vector, as shown in Fig. 4. Different from previous distillation works [19], [20] which impose the feature map alignment directly, we explicitly apply the domain-invariant regularization of the teacher and student networks in a uniform manner.

To enhance the performance and generalization ability of

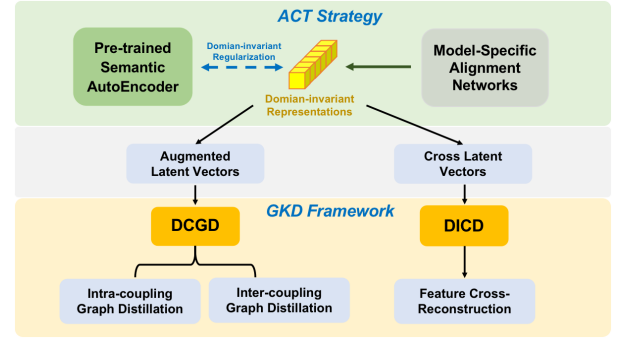


Fig. 2. Algorithm structure of the proposed Generalizable Knowledge Distillation (GKD) framework. The MSAN provides the semantic latent vectors. Based on the MSAN, the P-SAE provides the domain-invariant regularization for the semantic vectors in MSAN. Then, the domain-invariant latent vectors are obtained and employed to design the distillation schemes (DCGD + DICD) for effective and generalizable distillation.

the student network, two generalizable knowledge distillation schemas are proposed, named Dual Contrastive Graph Distillation (DCGD) and Domain-Invariant Cross Distillation (DICD). Specifically, in DCGD, we construct two implicit contrastive graphs based on the domain-invariant semantic latent vectors from MSAN. These two types of graphs could demonstrate the intra-coupling and inter-coupling semantic correlations through the various data augmentation tactics, as depicted in Fig. 3. We abandon the design of positive and negative coupling to characterize this ‘generalized knowledge’ as previous studies [29], [30], [51]. In contrast, the distillation of these implicit ‘contrastive graphs’ are more accessible to teacher-student distillation models. Moreover, our two contrastive graphs could represent more generalizable knowledge of distribution-shift caused by data perturbations in different couplings. We then propose a DICD schema to constrain the encoder and decoder of the student model respectively, more adapted with the generalizable semantic knowledge. In particular, the domain-invariant latent vectors encoded from MSAN are leveraged to cross-reconstruct the features by exchanging headers of TAN and SAN. The reconstructed features of student are fed into the decoder of the teacher to produce segmented predictions. The predictions are supervised by the original-predictions of the teacher. The similar operation is also done for the reconstructed teacher features. In such a paradigm, the decoder of the student model is cross-trained with its encoder simultaneously in this similar consistent pattern.

Furthermore, a new quantitative evaluation metric named Fréchet Semantic Distance (FSD) is tailored by the above-mentioned semantic autoencoder. We define the FSD as the Fréchet Distance between the latent features encoded by the student model (or teacher) and the P-SAE, respectively. We demonstrate that the proposed metric is plausible in estimating the domain-invariant semantic knowledge.

Overall, we detail the main contributions of this work:

- A generalizable knowledge distillation (GKD) framework is proposed for robust and efficient cross-domain medical image segmentation.

- The Model-Specific Alignment Networks (MSAN) incorporated with an Alignment Consistency Training (ACT) strategy are designed to obtain the domain-invariant representations.
- Two generalizable knowledge distillation schemes, named Dual Contrastive Graph Distillation (DCGD) and Domain-Invariant Cross Distillation (DICD) are proposed to boost the generalizable ability of student models.
- Extensive experiments on cross-domain medical image datasets verify that our method outperforms the previous knowledge distillation counterparts significantly. Remarkably, our method enforces the student to achieve competitive results compared with the complicated teacher model.

## II. RELATED WORK

### A. Efficient Medical Image Segmentation

Medical image segmentation has developed rapidly in recent years due to its significant practical values. Excessive research based on convolutional neural networks has been proposed for this task. Most of the previous work has focused on architectural optimization based on the UNet framework [1], which consists of the symmetric encoder and decoder. Valanarasu *et al.* [34] propose an over-complete architecture named Kiu-Net to map the deeper special features in blurred noisy MIS. Li *et al.* [35] introduce a dual-direction attention block for accurate retinal vessel segmentation. Since the inevitable significant increase in computational cost caused by deepening and widening the network architectures, lightweight techniques are introduced to remedy this issues. Zhou *et al.* [2] design an efficient ensemble strategy of various depth modules in UNet for better feature fusion. Perslev *et al.* [37] propose a two-phase Neural Architecture Search (NAS) framework for searching the lightweight models. However, these lightweight frameworks are limited in solving cross-domain problems. Though some works concentrate on investigating the generalizable ability of the network in cross-domain medical image segmentation. For example, Jiang *et al.* [4] apply a negative-transfer-resistant mechanism for cross-domain brain CT image segmentation. Their works fail to reasonably explore the combination of lightweight techniques and the generalization capabilities. Thus, in previous methods, lightweight frameworks always mean poor generalization. Conversely, our method aim to jointly improve the performance of lightweight models and enhance their generalizable abilities.

### B. Knowledge Distillation

Knowledge distillation provides the trade-off between network performance and computational cost. Conventionally, knowledge distillation aims to impart effective knowledge extracted from a complex teacher network to a shallow student network for improving the student performance [18]. Komodakis *et al.* [19] leverage the intermediate-layer attention maps transferred from teacher to student, which increases the capability significantly. Yim *et al.* [20] constrain the inner product between features from different layers of teacher and student, respectively. In addition, Liu *et al.* [21] define the ‘dark knowledge’ as the pair-wise and holistic-wise structural

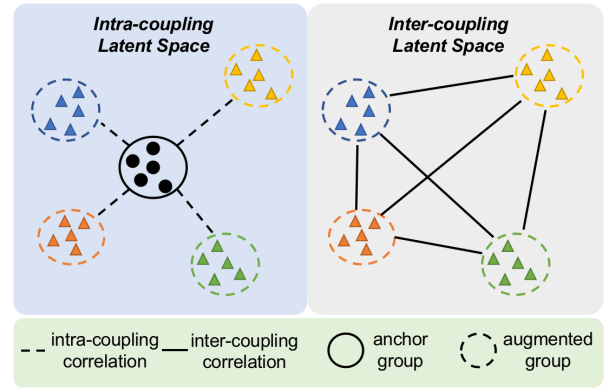


Fig. 3. Explanations of the intra-coupling and inter-coupling correlations for graph distillation. Circles  $\bigcirc$  represent anchor features. Triangles  $\triangle$  represent augmented features. Different colors represent different data perturbation tactics. We treat the different augmented data as different couplings. We try to calculate the intra-coupling correlations between the anchor features and each group of the augmented features. Meanwhile, as for augmented features, there are inter-coupling correlations among them. Through this design, we aim to replace the previous single sample representation from the perspective of data distribution.

graphs from a large network, which could address the sub-optimal challenge in the segmentation task. Besides, Wang *et al.* [22] extract the intra-class feature variation to guide the lightweight model training for obtaining better performance. Zou *et al.* [23] acquire the SOTA performance on pathological gastric cancer segmentation by enhancing the intermediate cross-layer correlation distilled from the teacher model. However, previous knowledge distillation methods only focus on the domain-specific task which bears poorly on cross-domain images. In contrast, we force the student to imitate the robust and generalizable knowledge from teacher via implicit contrastive graphs.

### C. Domain-invariant Representation

Since conventional knowledge distillation methods fail to transfer generalizable information, the approaches which engage in exploring domain-invariant knowledge attract enormous attention in the range of cross-domain tasks. Li *et al.* [28] extract the mean difference of the inter-domain features as the transferable domain-invariant representations to enhance the model generalizable ability. Creager *et al.* [38] design a general framework for domain-invariant learning to maximal informative for downstream invariant learning. Li *et al.* [39] leverage the graph learning to represent domain-invariant knowledge for few-shot domain adaptation. Moreover, some researchers introduce the contrastive learning based approaches to extract domain-invariant knowledge [30], [31]. He *et al.* [32] build a contrastive dynamic dictionary as domain-invariant features which facilitate the unsupervised vision tasks. Tian *et al.* [33] utilize the contrastive representation constructed by teacher model to distill lightweight student. You *et al.* [24] introduce two symmetric contrastive networks for weakly supervised medical image segmentation. Unlike the previous methods, which explicitly construct image-level positive-negative contrastive samples, the implicit contrastive



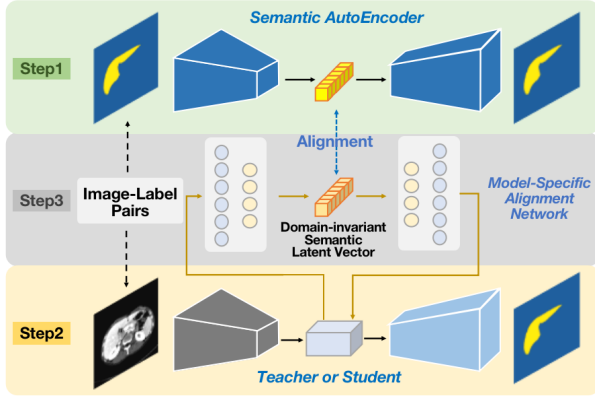


Fig. 4. Pipeline of our proposed Alignment Consistency Training (ACT) strategy for the Model-Specific Alignment Network (MSAN). Step 1: Obtain the Pre-trained Semantic AutoEncoder (P-SAE); Step 2: Train the teacher and student model respectively, only with task-driven supervision; Step 3: Train the Model-Specific Alignment Networks (TAN and SAN) of pre-trained teacher and pre-trained student models, respectively. Then the Domain-invariant Semantic Latent Vectors of each model could be obtained.

graphs involved in our method could represent more accessible generalizable knowledge for the student.

### III. PROPOSED METHOD

The proposed GKD framework aims at exploring the generalizable distillation knowledge, extracted from a powerful and complicated teacher model  $T$ , to improve the performance of the lightweight student model  $S$  on the medical image segmentation datasets. Additionally, the student model distilled by GKD achieves upgraded results on the other domain images, which could not be accessed in the training procedure. Sequentially, our GKD framework consists of three components: the Model-Specific Alignment Networks (MSAN), the Dual Contrastive Graph Distillation schema and the Domain-Invariant Cross Distillation (DICD) schema. For MSAN, we design a Pre-trained Semantic AutoEncoder (P-SAE) to provide the domain-invariant constraint, and propose an Alignment Consistency Training (ACT) strategy for network training. The algorithm description is illustrated in Fig. 2.

#### A. Model-Specific Alignment Networks

Model-Specific Alignment Networks consist of two alignment networks, Student Alignment Network (SAN) and Teacher Alignment Network (TAN), which are designed for the extraction of domain-invariant semantic latent vectors. As depicted in Fig. 4, our proposed MSAN is guided by the Alignment Consistency Training (ACT) strategy. By leveraging the ACT, the Pre-trained Semantic Autoencoder (P-SAE) is first introduced to provide the domain-invariant regularization for the above semantic latent vectors. Considering the holistic perceptive views, the encoded semantic features of teacher and student could be mapped to the regularized latent representations in MSAN. In this way, these semantic features could be treated as domain-invariant representations. More specifically, the details of ACT strategy are presented as below.

1) *Step 1: Obtain the Pre-trained Semantic Autoencoder:* Initially, given a domain-specific medical image  $X$  and a paired domain-invariant semantic annotation  $Y$ , the mapping from  $X$  to  $Y$  heavily relies on the semantic-aware features, which are extracted by the encoders of teacher and student. Thus, we introduce a Semantic AutoEncoder to explicitly provide the domain-invariant representations upon the semantic-aware features. Formally, the annotation  $Y$  is embedded to  $S^Y \in \mathbb{R}^{1 \times C}$  (the yellow vector in Fig. 4, Step 1), where  $C$  represents the vector dimension in the latent space. The Semantic Autoencoder is supervised by the semantic reconstruction loss, expressed as:

$$\mathcal{L}_{srec} = \|Y - \hat{Y}\|_1, \quad (1)$$

where  $\hat{Y}$  indicates the reconstructed mask by the autoencoder. In this way, we could obtain the Pre-trained Semantic AutoEncoder. The embedded  $S^Y$  is leveraged to provide the domain-invariant regularization in the following step 3.

2) *Step 2: Obtain the Scratch-trained Teacher and Student networks:* We find that in previous knowledge distillation researches [18], [22], simply transferring the prediction as knowledge from teacher to student is too ragged to learn for the student. Despite other works intend to distill the intermediate-layer knowledge [19]–[21], the deep-level semantic information in the bottleneck block after the teacher encoder would be neglected easily. Moreover, the spatial dimensions and channels of features at the bottleneck blocks of teachers and students are quite different, leading to inefficiency transfer [23]. In this paper, we transfer the bottleneck-level semantic information for shallow student networks. Therefore, in the step 2 of ACT, we provide the conventional semantic segmentation supervision for the scratch-trained teacher and student models. This stage engages in obtaining the encoded bottleneck-level semantic features from teacher and student. Then the parameters of the teacher and student models are fixed in the next step. The teacher and student are trained by the basic cross-entropy loss:

$$\mathcal{L}_{ce} = -\frac{1}{N} \sum (Y - \log(M^{T/S}(X))), \quad (2)$$

where  $M^{T/S}$  indicates the teacher or student models.

3) *Step 3: Obtain the Model-Specific Alignment Networks:* Driven by the aforementioned two steps, we develop the Model-Specific Alignment Networks (MSAN) for obtaining domain-invariant semantic latent vector, as shown in Fig. 4 (step 3). Structurally, the MSAN (TAN or SAN) consists of a pair of symmetrical encoding header and decoding header. Since the bottleneck-level semantic features  $F^T \in \mathbb{R}^{H' \times W' \times C'}$  and  $F^S \in \mathbb{R}^{H'' \times W'' \times C''}$  of these two networks are different on the spatial dimension, the encoding headers then map the features into the semantic latent vectors with a unified form, expressed as  $F^{T/S} \mapsto S^{T/S} \in \mathbb{R}^{1 \times C}$ . **Importantly**, we introduce the paired  $S^Y$  acquired from P-SAE for domain-invariant vector regularization. Thus, the  $S^{T/S}$  is constrained by  $S^Y$  as following:

$$\mathcal{L}_{regu} = \|S^Y - S^{T/S}\|_1. \quad (3)$$

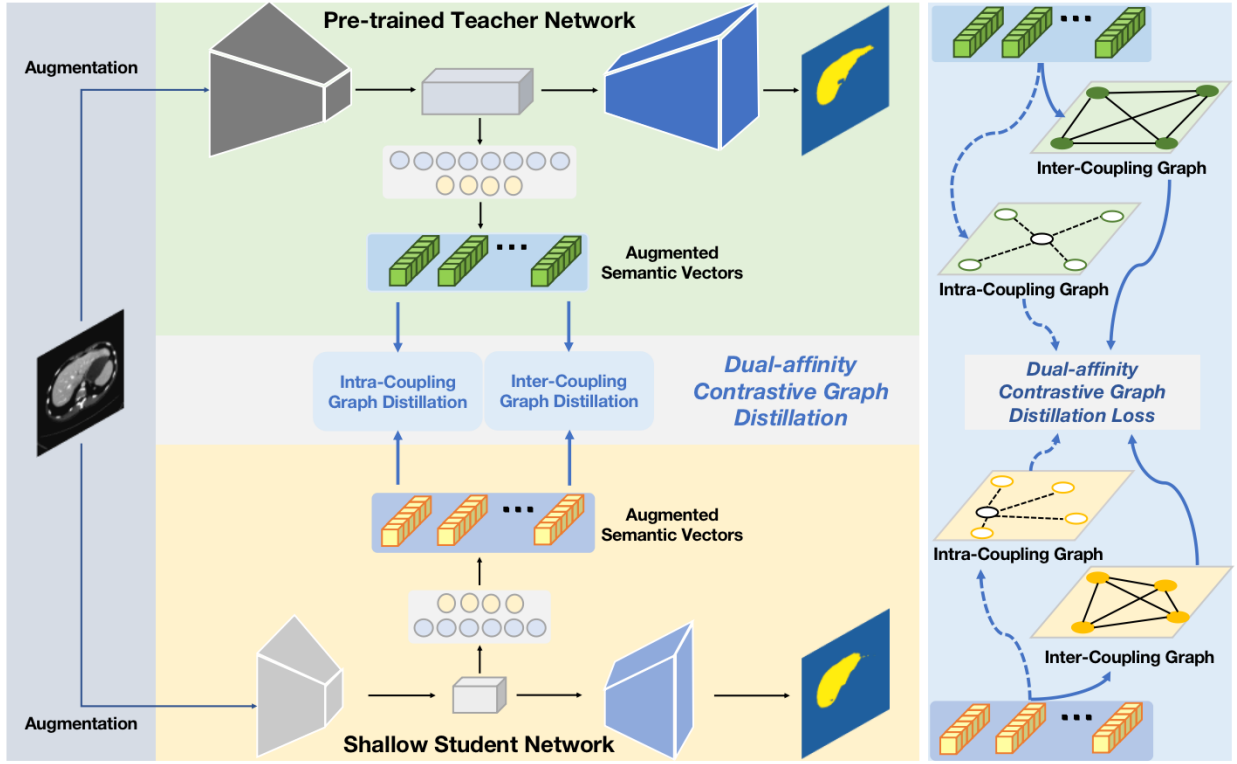


Fig. 5. The pipeline of our proposed Dual Contrastive Graph Distillation (DCGD) schema. Each training sample is fed into the two models simultaneously after several different data augmentation strategies jointly. The MSAN encoder is exploited to extract domain-invariant knowledge. We use the anchor vector and the augmented semantic vectors to construct the two types of contrastive graphs for distillation. Circles  $\bigcirc$  with black boundary in the right part represent the anchor vectors in the intra-coupling graph; others are augmented vectors in the different graphs. The pre-trained teacher network and MSAN structure are frozen when the student model is distilled at the training procedure.

Then, the semantic vectors are upsampled into feature maps by the model-specific decoding headers, which could also be treated as the feature map reconstruction to minimize the gap between the input and output of MSAN. This process is supervised by following loss:

$$\mathcal{L}_{rec}^{F^{T/S}} = \left\| F^{T/S} - \hat{F}^{T/S} \right\|_1 \quad (4)$$

where the  $\mathcal{L}_{rec}^{F^{T/S}}$  denotes feature reconstruction loss of MSAN. In this step, the overall MSAN is optimized by:

$$\mathcal{L}_{MSAN} = \mathcal{L}_{rec}^{F^{T/S}} + \lambda \mathcal{L}_{regu}, \quad (5)$$

$\lambda$  is the loss weight term which is set 0.5 in practice. Supervised by Eqn. (5), the encoded deep-level semantic features  $F^{T/S}$  from these two models are mapped to a consistent domain-invariant latent space. Thus, we could translate the domain-specific medical images into consistent domain-invariant vectors. After the training of MSAN, the encoder and decoder headers are fixed, and only the student model is scratch-optimized in the following Dual Contrastive Graph Distillation (DCGD) and Domain-Invariant Cross Distillation (DICD) schemes.

### B. Dual Contrastive Graph Distillation

Generally, in MIS tasks, deep network structure plays an important role for sufficient semantic information extraction.

Therefore, shallow student networks usually perform unsatisfactory than the complicated teacher networks, especially on cross-domain datasets. To transfer this precious knowledge from teacher to student, a direct idea to build the bridge is to enforce the spatial and dimensional feature alignment of the teacher and student. However, rough feature alignment (*i.e.* interpolation between feature maps of different spatial sizes) leads to semantic information loss, and hence the performance of the student model is limited [19], [23]. Meanwhile, the generalizable ability of student models is often overlooked. To this end, we jointly take these two factors into account, in order to achieve high-performance and generalizable improvements of the student networks. Benefiting from the predesignated MSAN, the features of these two models are aligned in a consistent domain-invariant pattern. To further investigate the generalizable knowledge representation, we propose a Dual Contrastive Graph Distillation (DCGD) schema. It is worth noting that in DCGD, the contrastive graphs implicitly introduce more knowledge about the data distribution than the representation of a single sample, which could bring more generalization and robustness. Specifically, the sample  $X$  is firstly augmented by various tricks (*i.e.* Random Cutout, Sobel Filter, Gaussian noise, Gaussian blur), which expressed as:  $X \mapsto \mathbb{X} = \{\hat{x}, x_1, x_2, \dots, x_i\}$ , where  $\hat{x}$  represents the original anchor sample and  $x_i$  denotes the  $i$ -th augmented sample. For anchor sample and each augmented

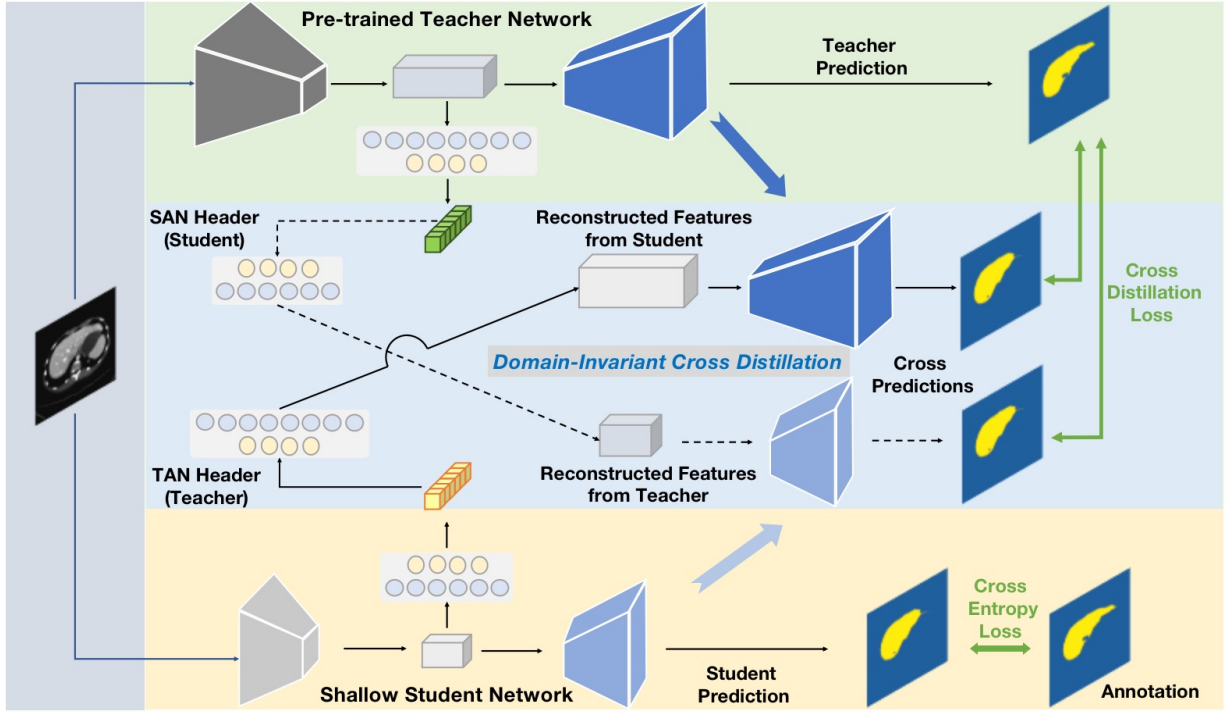


Fig. 6. The pipeline of our proposed Domain-Invariant Cross Distillation (DICD) schema. In DICD, the model-specific features from teacher and student are cross-reconstructed by the header exchanging of MSAN. The pre-trained teacher model is utilized to provide the cross distillation supervision on both the encoder and decoder of the student respectively.

sample, there are different contrastive couplings composed as  $\mathcal{C} = \{(\hat{x}, x_1), (\hat{x}, x_2), \dots, (\hat{x}, x_i)\}$ . We feed the  $\mathbb{X}$  into the both models (*i.e.* teacher and student) simultaneously and construct two implicit contrastive graphs to represent the generalizable knowledge. As shown in Fig. 5, our DCGD schema consists of two sub-distillation methods: (i) the intra-coupling Contrastive Graph Distillation and (ii) the inter-coupling Contrastive Graph Distillation.

1) *Intra-coupling Contrastive Graph Distillation:* With the various data augmentation strategies, the teacher and student models both receive  $\mathbb{X} = \{\hat{x}, x_1, x_2, \dots, x_i\}$  as the inputs. Intuitively, for each  $x_i$  in  $\mathbb{X}$ , the different data augmentations on the anchor  $\hat{x}$  result in different distribution shifts of the semantic margin on the domain-specific medical images, as shown in Fig. 3. From another perspective, the encoder of teacher networks could obtain more robust and generalizable representations with different augmented  $x_i$ . Since the annotation of  $x_i$  is difficult to obtain for supervision, we aim to construct the **implicit contrastive graphs** in the semantic latent space for intermediate distillation. These implicit contrastive graphs represent the semantic-shift between  $\hat{x}$  and various  $x_i$  in the different couplings  $\mathcal{C} = \{(\hat{x}, x_1), (\hat{x}, x_2), \dots, (\hat{x}, x_i)\}$ . Therefore, the intra-coupling contrastive graph is formulated as  $\mathcal{G}_{intra} < \mathcal{N}, \mathcal{E} >$ . Where  $\mathcal{N}$  indicates the nodes in the graph;  $\mathcal{E}$  denotes the edges between the anchor node  $\mathcal{N}_{\hat{x}}$  (from  $\hat{x}$ ) and the augmented nodes  $\mathcal{N}_{x_i}$  (from  $x_i$ ) in different couplings.  $\mathcal{N}_{\hat{x}}$  and  $\mathcal{N}_{x_i}$  are embedded by MSAN encoding headers  $\mathbb{E}_{MSAN}^{T/S}(\cdot)$  of teacher and student, respectively. More specifically, the anchor sample  $\hat{x}$  and each augmented sample

$x_i$  with different couplings are firstly fed into the pre-trained teacher and scratch-trained student encoders to obtain the model-specific features as expressed:  $\mathbb{E}^{T/S}(\hat{x}) \mapsto F_{\hat{x}}^{T/S}$  or  $\mathbb{E}^{T/S}(x_i) \mapsto F_{x_i}^{T/S}$ . Then, we leverage the fixed  $\mathbb{E}_{MSAN}^{T/S}$  to embed the model-specific features into the domain-invariant semantic latent vectors:  $\mathbb{E}_{MSAN}^{T/S}(F_{\hat{x}}^{T/S}) \mapsto S_{\hat{x}}^{T/S} \in \mathbb{R}^{1 \times C}$  or  $\mathbb{E}_{MSAN}^{T/S}(F_{x_i}^{T/S}) \mapsto S_{x_i}^{T/S} \in \mathbb{R}^{1 \times C}$ , where  $C = 512$  in practice. Therefore, in  $\mathcal{G}_{intra}$ , we intend to transfer the intra-coupling semantic-shift of the teacher model caused by data perturbation. Further, the  $S_{x_i}^{T/S}$  and  $S_{\hat{x}}^{T/S}$  are transposed to  $\mathbb{R}^{C \times 1}$ , and the matrix multiplications are employed to obtain the  $512 \times 512$  intra-coupling similarity maps as the graph nodes  $\mathcal{N}_{\hat{x}/x_i}^{T/S} \in \mathbb{R}^{C \times C}$ . As illustrated in Fig. 5, we calculate the cosine similarity between the  $\mathcal{N}_{\hat{x}}^{T/S}$  and each  $\mathcal{N}_{x_i}^{T/S}$  with different couplings as the edges  $\mathcal{E}^{T/S}$  in  $\mathcal{G}_{intra}$ . Finally, we exploit the  $L_1$  loss to transfer the generalizable knowledge from teacher to student:

$$\mathcal{L}_{intra} = \mathcal{L}_{intra}(\mathcal{N}) + \mathcal{L}_{intra}(\mathcal{E})$$

$$\left\| \mathcal{N}_{\hat{x}/x_i}^T - \mathcal{N}_{\hat{x}/x_i}^S \right\|_1 + \left\| \mathcal{E}^T - \mathcal{E}^S \right\|_1 \quad (6)$$

In Eqn. (6), the implicit semantic intra-coupling contrastive graph distillation is expressed. When  $\mathcal{L}_{intra}$  is utilized, the student networks are reinforced to mimic the semantic and generalizable representative abilities of the teacher.

2) *Inter-coupling Contrastive Graph Distillation:* Furthermore, we propose the inter-coupling contrastive graph  $\mathcal{G}_{inter} < \mathcal{N}, \mathcal{E} >$  to represent the inter-coupling semantic-shift among the each node as illustrated in Fig. 3. In  $\mathcal{G}_{inter}$ , all

the  $\mathcal{N}$  are encoded from augmented samples  $x_i$  with different couplings as shown in Fig. 5. We argue that as for different  $x_i$ , there are inter-coupling semantic-shift caused by different data perturbations, which bring more robust and generalizable information from the perspective of data distribution. The  $\mathcal{G}_{inter}$  aims to formulate the correlations between different augmented nodes as this generalizable knowledge transferred to the student. Since in different couplings  $(\hat{x}, x_i)$ , they have shared anchor vector. We directly leverage the augmented domain-invariant semantic latent vectors  $S_{x_i}^{T/S} \in \mathbb{R}^{1 \times C}$  as graph nodes  $\mathcal{N}_{x_i}^{T/S}$ . Moreover, the inter-graph edges  $\mathcal{E}^{T/S}$  are calculated among every  $\mathcal{N}_{x_i}^{T/S}$  as cosine-similarity. In contrast with intra-coupling graph distillation, we regularize each nodes with the softmax function and then conduct the Kullback-Leibler Divergence between the  $\mathcal{N}_{x_i}^T$  and  $\mathcal{N}_{x_i}^S$ , expressed as:

$$\mathcal{L}_{inter}(\mathcal{N}) = KL(\text{soft}(\mathcal{N}_{x_i}^T) \parallel \text{soft}(\mathcal{N}_{x_i}^S)), \quad (7)$$

where  $\text{soft}(\cdot)$  indicates the softmax operation. Meanwhile, we utilize the  $L_1$  loss to constraint with paired inter-graph edges.

$$\mathcal{L}_{inter}(\mathcal{E}) = \|\mathcal{E}^T - \mathcal{E}^S\|_1. \quad (8)$$

In summary, the inter-coupling contrastive graph distillation is supervised by:

$$\mathcal{L}_{inter} = \mathcal{L}_{inter}(\mathcal{N}) + \mathcal{L}_{inter}(\mathcal{E}). \quad (9)$$

### C. Domain-Invariant Cross Distillation

To further improve the performance of the student model, we propose a Domain-Invariant Cross Distillation (DICD) schema based on the aforementioned MSAN as shown in Fig. 6. We notice that a powerful decoder which can be adaptive with generalizable encoded features also plays a crucial role in cross-domain MIS tasks. To this end, we enhance the encoder and decoder of the student model jointly, in a cross-training manner.

To be specific, we aim to leverage the cross-reconstructed features to impose the consistency constraint on the network predictions. Guided by MSAN, we obtain the regularized domain-invariant semantic latent vectors  $S_{\hat{x}}^{T/S} \in \mathbb{R}^{1 \times C}$  from  $F_{\hat{x}}^{T/S}$ . Since the input feature dimensions of these two network decoders (*i.e.* teacher and student) are different, we utilize the pre-trained MSAN decoding headers to obtain the cross-reconstructed features  $\hat{F}_{\hat{x}}^{T/S}$  from  $S_{\hat{x}}^{S/T}$  formulated as:

$$\begin{aligned} \hat{F}_{\hat{x}}^T &= \mathbb{D}_{TAN}(S_{\hat{x}}^S) \\ \hat{F}_{\hat{x}}^S &= \mathbb{D}_{SAN}(S_{\hat{x}}^T), \end{aligned} \quad (10)$$

where  $\mathbb{D}_{TAN}$  and  $\mathbb{D}_{SAN}$  represent the MSAN decoding headers of Teacher (T) and Student (S). Afterwards, the cross-reconstructed  $\hat{F}_{\hat{x}}^{T/S}$  are fed into the exchanged network decoders to produce predictions  $(\mathbb{D}^{T/S}(\hat{F}_{\hat{x}}^{T/S}) \mapsto \hat{Y}_{rec}^{T/S})$ , respectively. Then, we exploit the segmentation result  $Y^{T/S}$  from original features to provide the  $L_1$  constraint on the predictions from cross-constructed features, separately. As expressed below:

$$\mathcal{L}_{DICD} = \|Y^T - \hat{Y}_{rec}^T\|_1 + \|Y^S - \hat{Y}_{rec}^S\|_1. \quad (11)$$

With the proposed DICD, the student model receives more cross-reconstructed features from teacher to further improve the segmentation performance and pursue more generalizable ability. Meanwhile, in DICD, the student model is also supervised by basic cross-entropy loss  $\mathcal{L}_{ce}$ . Notably, our DICD is only conducted on the anchor vectors of the two models.

### D. Objective Functions

The optimization of our proposed generalizable knowledge distillation (GKD) framework can be divided into 3 phases. Firstly, the teacher and student models are trained by  $\mathcal{L}_{ce}$ , while the parameters of teacher model are frozen in the following phases. Then, we employ the  $\mathcal{L}_{MSAN}$  to train the MSAN of both two models which only the parameters of MSAN are updated in this phase. In the last phase, we aim at obtaining the scratch-trained student model based on the aforementioned pre-trained teacher model and MSAN. The total training loss  $\mathcal{L}_{total}$  is expressed as:

$$\mathcal{L}_{total} = \mathcal{L}_{ce} + \alpha\mathcal{L}_{intra} + \beta\mathcal{L}_{inter} + \gamma\mathcal{L}_{DICD}, \quad (12)$$

where the hyper-parameters  $\alpha$ ,  $\beta$  and  $\gamma$  are set as 100, 100, 0.5 in practice, respectively.

## IV. EXPERIMENTS

### A. Datasets

1) *Liver Segmentation Datasets*: We conduct extensive experiments on the CHAOS [40] and LITS [41] liver segmentation datasets as depicted in Fig. 1. We focus on the CT modality images in the CHAOS liver segmentation dataset to verify our proposed GKD framework. CHAOS contains CT liver images of 40 patients whose livers are **healthy and not diseased**. In the original CHAOS liver segmentation dataset, both the training and testing sets contain images of 20 patients. However, only the original training set provides binary-class ground truth. We choose 13 patient images (*i.e.* patient number: 1, 2, 5, 6, 8, 10, 14, 16, 18, 19, 21, 22, 23) from the original training set as the sub-training set for this experiment, and the remaining 7 patient images (*i.e.* patient number: 24, 25, 26, 27, 28, 29, 30) are used as the sub-testing set. Thus, we obtain 1,578 CT liver images as the sub-training set and 1,296 CT liver images as the sub-testing set. Each CT image in CHAOS has  $512 \times 512$  spatial size. Moreover, we introduce the LITS liver segmentation dataset to verify the generalizable ability of the distilled student by our proposed GKD. The original LITS dataset contains numerous CT liver images of **diseased patients**, which is challenging due to the uneven shape and diffuseness of the images. Randomly, we pick 1,000 liver images with ground truth from LITS and merge their semantic categories into two categories: liver and background. The selected liver images are leveraged as a generalization test set which is not involved in the training stage. All the images in LITS have  $256 \times 256$  spatial size.

2) *Retinal Vessel Segmentation Datasets*: We also introduce three retinal vessel segmentation datasets CHASEDB1 [42], STARE [43] and DRIVE [44] in the experiments to evaluate our proposed GKD framework. The CHASEDB1 dataset consists of 24 retinal images with a spatial size of  $999 \times 960$ .



TABLE I

COMPARISON RESULTS ON CHAOS AND LITS DATASETS. ALL THE MODELS ARE ONLY TRAINED ON THE CHAOS DATASET, AND DIRECTLY TESTED ON BOTH DATASETS.  $\uparrow$  INDICATES THE HIGHER, THE BETTER.  $\downarrow$  INDICATES THE LOWER, THE BETTER.

Model	SE $\uparrow$			ACC $\uparrow$			AUC $\uparrow$			F1 $\uparrow$			mIOU $\uparrow$		
	CHAOS	LITS	GAP $\downarrow$	CHAOS	LITS	GAP $\downarrow$	CHAOS	LITS	GAP $\downarrow$	CHAOS	LITS	GAP $\downarrow$	CHAOS	LITS	GAP $\downarrow$
<b>T: FANet</b>	<b>0.9613</b>	<b>0.8356</b>	<b>0.1257</b>	<b>0.9932</b>	<b>0.9835</b>	<b>0.0097</b>	<b>0.9986</b>	<b>0.9908</b>	<b>0.0078</b>	<b>0.9401</b>	<b>0.8647</b>	<b>0.0754</b>	<b>0.9399</b>	<b>0.8721</b>	<b>0.0678</b>
S: Mobile Unet	0.8840	0.4812	0.4028	0.9899	0.9625	0.0274	0.9972	0.9723	0.0249	0.9057	0.6180	0.2877	0.9085	0.7042	0.2043
KD	0.9349	0.7296	0.2053	0.9883	0.9734	0.0149	0.9971	0.9847	0.0124	0.8979	0.7755	0.1224	0.9012	0.8027	0.0985
AT	0.9394	0.7212	0.2182	0.9893	0.9737	0.0156	0.9973	0.9805	0.0168	0.9062	0.7757	0.1305	0.9086	0.8030	0.1056
FSP	0.9320	0.7140	0.2180	0.9912	0.9740	0.0172	0.9973	0.9873	0.0100	0.9209	0.7763	0.1446	0.9220	0.8036	0.1184
SKD	0.9363	0.7983	0.1380	0.9901	0.9764	0.0137	0.9977	0.9863	0.0114	0.9121	0.8103	0.1018	0.9139	0.8281	0.0858
IFVD	0.9250	0.7175	0.3075	0.9907	0.9752	0.0155	0.9977	0.9843	0.0134	0.9164	0.7851	0.1313	0.9180	0.8101	0.1079
CoCo	0.9255	0.7292	0.1933	0.9917	0.9764	0.0153	0.9980	0.9783	0.0197	0.9251	0.7960	0.1291	0.9260	0.8182	0.1078
<b>GKD</b>	<b>0.9451</b>	<b>0.8251</b>	<b>0.1200</b>	<b>0.9924</b>	<b>0.9825</b>	<b>0.0099</b>	<b>0.9984</b>	<b>0.9912</b>	<b>0.0072</b>	<b>0.9320</b>	<b>0.8560</b>	<b>0.0760</b>	<b>0.9323</b>	<b>0.8649</b>	<b>0.0674</b>

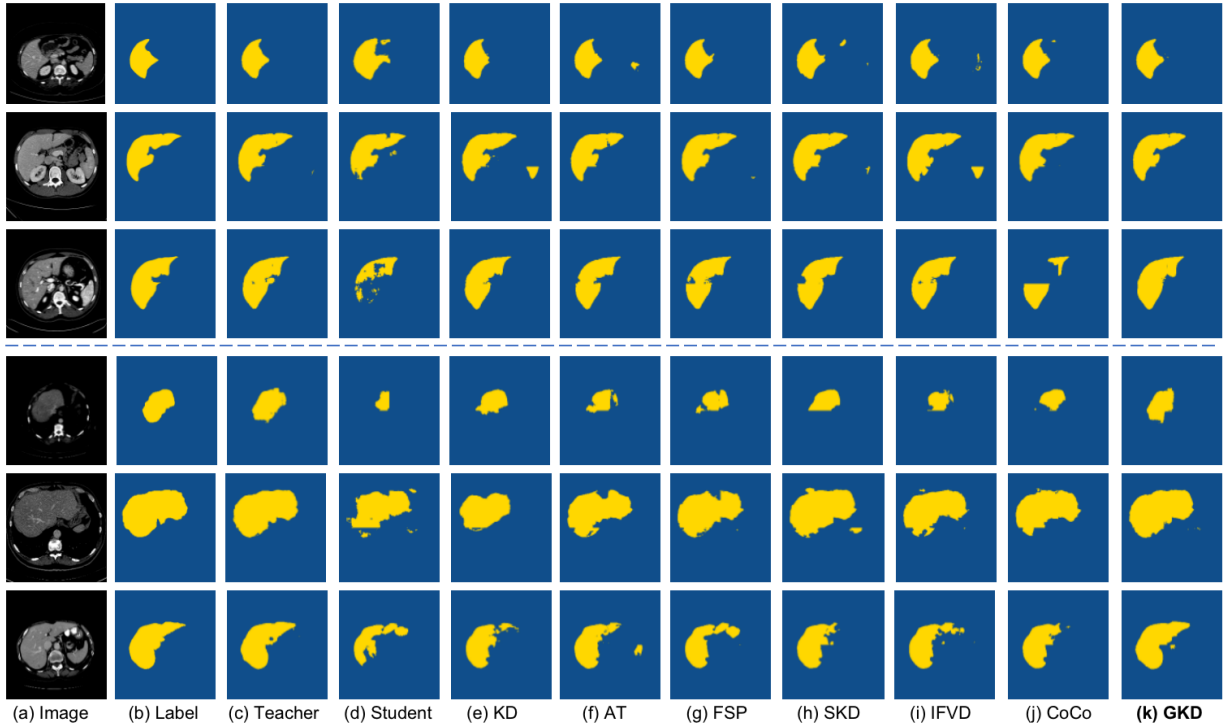


Fig. 7. Liver segmentation visual comparisons of our proposed GKD with state-of-the-art knowledge distillation counterparts and labels. The top three-row samples are from the CHAOS dataset, and the bottom three-row samples are from the LITS dataset. Notably, all the models are trained on the CHAOS dataset and directly tested on both two datasets.

The images are from the left and right eyes of 14 children. We select the retinal vessel images of the first 7 children as the training set and the remaining images as the test set. The STARE dataset contains 20 retinal vessel images with a spatial size of  $700 \times 604$ . Followed by previous work [35], we directly evaluate the generalizable ability of student model on the last 10 images. The DRIVE dataset includes 40 images of retinal vessels, each with a spatial size of  $565 \times 584$ . Similarly, we employ the 20 testing images of DRIVE dataset as the generalization testing set to verify our proposed GKD framework.

Notably, we only involve CHAOS and CHASEDB1 datasets in the training phase to obtain the student model and test directly on the other datasets. Besides, all the images are cropped into  $128 \times 128$  size patches as the model input.

## B. Evaluation Metrics

1) *Metrics on Semantic Segmentation:* We adopt various metrics to evaluate the segmentation performance of the proposed GKD framework, including Sensitivity/Recall (dubbed SE), pixel Accuracy (ACC), AUC (the under area of receiving operator characteristics (ROC) curve) [45], F1 score and mIOU. Since the liver and retinal vessel segmentation tasks are more focused on the foreground semantic classes (*i.e.* the liver and vessel pixels), we treat the SE as the main metric. Additionally, we introduce the Floating-point Operations Per second (FLOPs) and the network Parameters (Params) to measure the model complexity in our experiments.

2) *Fréchet Semantic Distance:* To further evaluate the generalizable ability of the student model optimized by our



TABLE II

RESULTS ON CHASEDB1, STARE AND DRIVE DATASETS. ALL THE MODELS ARE ONLY TRAINED ON THE CHASEDB1 DATASET, AND DIRECTLY TESTED ON THREE RETINAL VESSEL DATASETS.  $\uparrow$  INDICATES THE HIGHER, THE BETTER.

Model	SE $\uparrow$			ACC $\uparrow$			AUC $\uparrow$			F1 $\uparrow$			mIOU $\uparrow$		
Dataset	CHASEDB1	STARE	DRIVE	CHASEDB1	STARE	DRIVE	CHASEDB1	STARE	DRIVE	CHASEDB1	STARE	DRIVE	CHASEDB1	STARE	DRIVE
T: FANet	<b>0.8103</b>	<b>0.6485</b>	<b>0.5444</b>	<b>0.9730</b>	<b>0.9544</b>	<b>0.9597</b>	<b>0.9836</b>	<b>0.9541</b>	<b>0.9561</b>	<b>0.7711</b>	<b>0.6526</b>	<b>0.6558</b>	<b>0.7996</b>	<b>0.7183</b>	<b>0.7229</b>
S: Mobile Unet	<b>0.6894</b>	<b>0.5050</b>	<b>0.4174</b>	0.9686	0.9575	0.9543	0.9737	0.9244	0.9320	0.7113	0.6106	0.5630	0.7596	0.6977	0.6723
KD	0.6921	0.4958	0.3855	0.9715	0.9608	0.9538	0.9800	0.9425	0.9450	0.7315	0.6254	0.5410	0.7735	0.7072	0.6617
AT	0.7150	0.5391	0.4277	0.9716	0.9598	0.9551	0.9788	0.9391	0.9377	0.7385	0.6391	0.5732	0.7779	0.7139	0.6777
FSP	0.7345	0.5193	0.4125	0.9698	0.9587	0.9548	0.9770	0.9213	0.9258	0.7320	0.6242	0.5631	0.7729	0.7055	0.6727
SKD	0.7478	0.5677	0.4515	0.9701	0.9584	0.9570	0.9792	0.9300	0.9106	0.7369	0.6434	0.5972	0.7761	0.7155	0.6907
IFVD	0.7264	0.5627	0.4536	0.9716	0.9608	0.9564	0.9786	0.9351	0.9311	0.7421	0.6551	0.5947	0.7802	0.7232	0.6890
CoCo	0.7323	0.5644	0.4531	0.9723	0.9586	0.9566	0.9799	0.9391	0.9237	0.7476	0.6646	0.5958	0.7840	0.7273	0.6897
GKD	<b>0.7804</b>	<b>0.6252</b>	<b>0.5061</b>	<b>0.9728</b>	<b>0.9612</b>	<b>0.9582</b>	<b>0.9837</b>	<b>0.9504</b>	<b>0.9490</b>	<b>0.7637</b>	<b>0.6803</b>	<b>0.6309</b>	<b>0.7940</b>	<b>0.7375</b>	<b>0.7087</b>

proposed GKD, we design a **new quantitative metric** named Fréchet Semantic Distance (FSD). In the aforementioned ACT, we introduce a pre-trained semantic autoencoder (P-SAE) in self-supervised manner. Accordingly, we argue that the P-SAE can be treated as a domain-invariant semantic feature extractor. Inspired by FID [46] metric which exploits the pre-trained Inception-v3 [47] network as feature extractor. We define the FSD as the Fréchet distance between the latent features extracted from P-SAE and pre-trained MSAN encoding headers, respectively. Specifically, the distance is formulated as Gaussian mean and covariance of both features as follows:

$$FSD(X, Y) = \|\mu_x - \mu_y\| + Tr(\sum_x + \sum_y - 2(\sum_x \sum_y)^{1/2}) \quad (13)$$

where  $X$  and  $Y$  are the sampled input images and the paired labels for MSAN and P-SAE, respectively.  $\mu_x$  and  $\mu_y$  are Gaussian mean of extracted features;  $\sum_x$  and  $\sum_y$  are covariance of extracted features. Different from previous [46], our FSD aims to evaluate the effectiveness of domain-invariant semantic knowledge.

### C. Implementation Details

To demonstrate the priority of our proposed GKD framework, we adopt FANet [35] as the powerful teacher model which shows SOTA performance on these medical image segmentation tasks. Moreover, we employ the various lightweight models (*i.e.* MobileNetv2 [48], ENet [49]) as students to verify the generalization of our framework. We take the MobileNetv2 as the main student model in the following experiments. All the models are implemented on the Pytorch [50] platform with 2 NVIDIA TITAN XP GPUs. The batchsize is set to 16 for both teacher and student networks. In the training phase, we adopt the initial learning rate as 0.003 and the total optimization epoch is 100.

### D. Comparative Experiments

1) *Experiments on Liver Segmentation Task:* We compare our method with various knowledge distillation approaches: KD [18], AT [19], FSP [20], SKD [21], IFVD [22], CoCo [23]. As reported in Table. I, our proposed GKD outperforms these various knowledge distillation methods with a large margin on liver segmentation tasks. All the models in Table. I are trained

only on the CHAOS dataset. We directly test the models on the LITS dataset to demonstrate the priority of both high performance and generalizable ability. More specifically, to evaluate the generalizable ability of our GKD, we calculate the performance **GAP** between these two datasets. As for the teacher model, due to its complicated network architecture, there is a slight drop in performance when testing directly on the LITS dataset. However, the original shallow student model suffers from low-preciseness in the LITS testing phase. Although the previous distillation methods obtain the apparent performance improvement in the CHAOS testing phase. They still fail at generalization testing on the LITS dataset. In contrast, our GKD achieves competitive performance with teacher model on AUC evaluation indicator in LITS testing phase (*i.e.* GKD 0.9912 *vs* Teacher 0.9908). Remarkably, as for performance **GAP** between testing phase on CHAOS and LITS, our proposed GKD even reach better results than teacher model with several evaluation indicators (*i.e.* SE: GKD 0.1200 *vs* Teacher 0.1257; AUC: GKD 0.0072 *vs* Teacher 0.0078; mIOU: GKD 0.0674 *vs* Teacher 0.0678). The narrowed performance gap fully verifies the effectiveness of our proposed method for improving the generalization ability of the student network.

Additionally, from the perspective of qualitative evaluation, we show the visual comparison results predicted by various distillation methods and our proposed GKD in Fig. 7. Obviously, the image structures and textures of the CHAOS dataset and the LITS dataset are quite different. While the other distillation methods fail to segment the liver foreground and distinguish background pixels correctly, our method consistently surpass the counterparts on cross-domain scenes.

2) *Experiments on Retinal Vessel Segmentation Task:* As reported in Tabel. II, we further conduct the competitive experiments on retinal vessel segmentation tasks. In this phase, we introduce three datasets to verify the high segmentation performance and generalizable ability of our proposed GKD. Similarly, all the models involved in these experiments are trained on the CHASEDB1 training set and directly tested on the three vessel segmentation datasets. Our method achieves superior performance compared with other distillation ones [18]–[24]. Quantitatively, as for SE indicator, the proposed GKD outperforms the scratch-trained student model by a large margin of 13.2% (*i.e.*  $(0.7804 - 0.6894)/0.6894 \approx 13.2\%$ , colored in blue for better view.) on the CHASEDB1

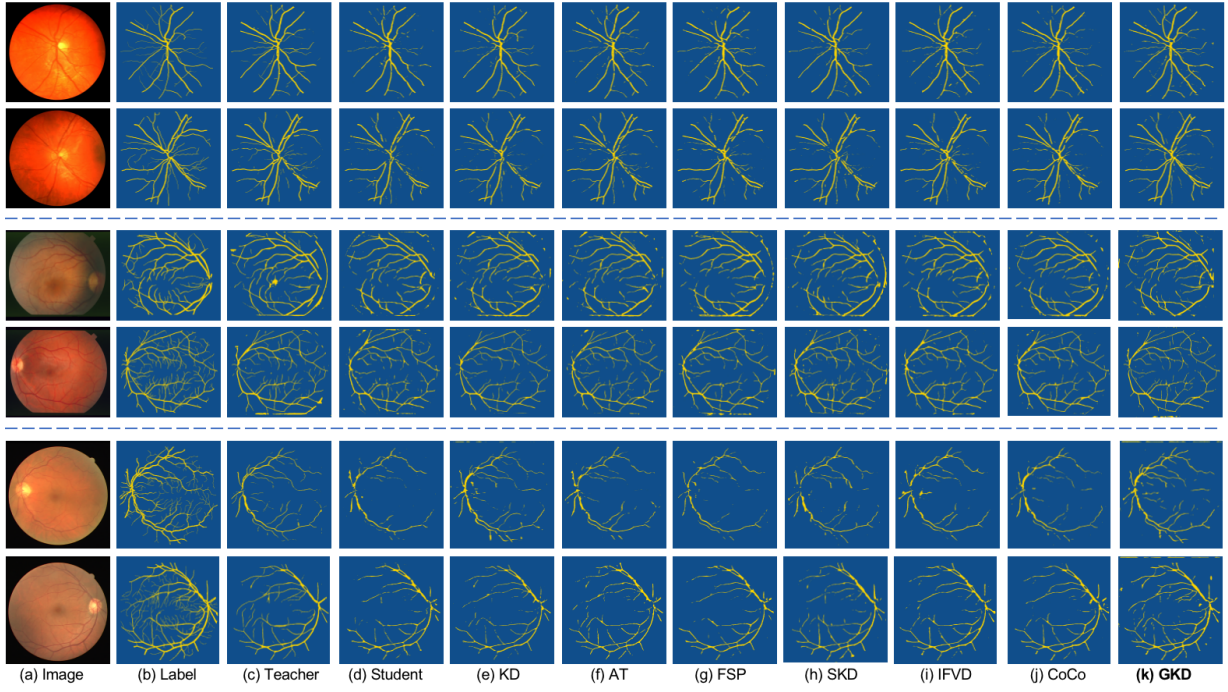


Fig. 8. Retinal vessel segmentation visual comparisons of our proposed GKD with previous knowledge distillation counterparts. The top two-row samples are from the CHASEDB1 dataset, the middle two-row samples are from the STARE dataset, and the bottom two-row samples are from the DRIVE dataset. Notably, all the models are trained on the CHASEDB1 dataset and directly tested on the three testing sets.

TABLE III  
ABLATION STUDY ON CHAOS AND LITS DATASETS.  $\uparrow$  INDICATES THE HIGHER, THE BETTER.  $\downarrow$  INDICATES THE LOWER, THE BETTER.

Model	Dataset	SE $\uparrow$	ACC $\uparrow$	AUC $\uparrow$	F1 $\uparrow$	mIOU $\uparrow$
<b>T: FANet</b>	CHAOS	0.9536	0.9928	0.9985	0.9361	0.9362
	LITS	0.8251	0.9825	0.9872	0.8556	0.8646
	GAP $\downarrow$	0.1285	0.0103	0.0113	0.805	0.0716
S: Mobile Unet	CHAOS	0.8840	0.9899	0.9972	0.9057	0.9085
	LITS	0.4812	0.9625	0.9723	0.6180	0.7042
	GAP $\downarrow$	0.4028	0.0274	0.0249	0.2877	0.2043
S: w/ Intra	CHAOS	0.9194	0.9911	0.9978	0.9189	0.9203
	LITS	0.6831	0.9747	0.9876	0.7730	0.8018
	GAP $\downarrow$	<b>0.2363</b>	0.0164	0.0102	0.1459	0.1185
S w/ Intra + Inter	CHAOS	<b>0.9474</b>	0.9915	0.9983	0.9244	0.9252
	LITS	0.7632	0.9780	0.9882	0.8145	0.8320
	GAP $\downarrow$	<b>0.1842</b>	0.0135	0.0101	0.1099	0.0932
<b>S w/ Intra + Inter + Cross</b>	CHAOS	0.9451	<b>0.9924</b>	<b>0.9984</b>	<b>0.9320</b>	<b>0.9323</b>
	LITS	<b>0.8251</b>	<b>0.9825</b>	<b>0.9912</b>	<b>0.8560</b>	<b>0.8649</b>
	GAP $\downarrow$	<b>0.1200</b>	<b>0.0099</b>	<b>0.0072</b>	<b>0.0760</b>	<b>0.0674</b>

dataset. Moreover, as for the testing phase on STARE and DRIVE, the GKD improves the SE indicator by about 23.8% (*i.e.*  $(0.6252 - 0.5050)/0.5050 \approx 23.8\%$ ) and 21.3% (*i.e.*  $(0.5061 - 0.4174)/0.4174 \approx 21.3\%$ ) compared with scratch-trained student. Besides, our GKD even achieves better results than teacher model with several evaluation indicators such as ACC, F1 score, and mIOU in the STARE testing phase (*i.e.* ACC: 0.9612 *vs* 0.9544; F1: 0.6803 *vs* 0.6526; mIOU: 0.7375 *vs* 0.7183).

Qualitatively, we illustrate the visual comparison results segmented by other distillation counterparts and our GKD in Fig. 8. It is obvious that there are domain gaps (*i.e.* illumination) among the three datasets. To be specific, the retinal vessel images in the CHASEDB1 dataset are much more bright-some than another two datasets. In addition, the different shooting angles also lead to variability in vessel structure and texture. The aforementioned domain-gap results in a large margin decline of other compactors when directly testing on STARE and DRIVE. On the contrary, the last column in Fig. 8 demonstrates that our method has a stronger generalizable ability than previous ones [18]–[24]. Notably, our introduced liver and retinal vessel segmentation tasks have different image textures and modalities, which further demonstrates the migration ability of our proposed method.

### E. Ablation Study

In this subsection, we conduct the ablation study on the key distillation constraints of our GKD. For brevity, we report the experimental results over 5 testing datasets (*i.e.* two liver segmentation datasets and three retinal vessel segmentation datasets), simultaneously.

1) *Ablation on Intra-coupling Graph Distillation:* Quantitatively, we analyze the impact of the proposed Intra-coupling Graph Distillation schema on both liver segmentation and retinal vessel segmentation tasks. Our intra-coupling graph demonstrates the semantic-shift between the anchor features and each augmented features with different couplings, caused by data augmentation. By enforcing the student to mimic representative vectors of teacher in the regularized latent space,

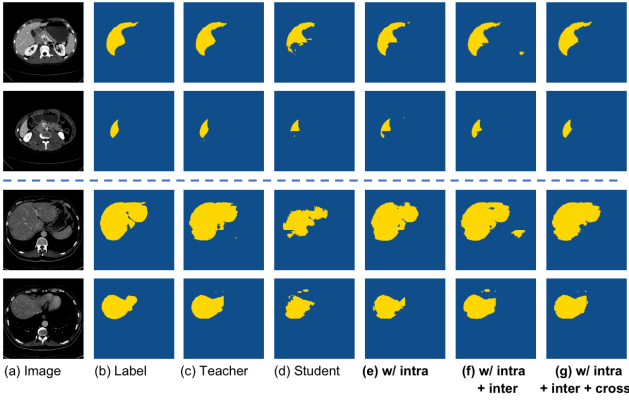


Fig. 9. The visual comparisons of ablation study on the liver segmentation task. The top two-row samples are from CHAOS dataset, and the bottom two-row samples are from the LITS dataset. Notably, all the models are trained on the CHAOS dataset and directly tested on these two datasets.

TABLE IV  
ABLATION STUDY ON CHASEDB1, STARE AND DRIVE DATASETS.  $\uparrow$  INDICATES THE HIGHER, THE BETTER.

Model	Dataset	SE $\uparrow$	ACC $\uparrow$	AUC $\uparrow$	F1 $\uparrow$	mIOU $\uparrow$
<b>T: FANet</b>	CHASEDB1	0.8102	0.9730	0.9836	0.7711	0.7996
	STARE	0.6485	0.9544	0.9541	0.6526	0.7183
	DRIVE	0.5444	0.9697	0.9561	0.6558	0.7229
S: Mobile Unet	CHASEDB1	0.6894	0.9686	0.9737	0.7113	0.7596
	STARE	0.5050	0.9575	0.9244	0.6106	0.6977
	DRIVE	0.4174	0.9543	0.9320	0.5630	0.6723
S; w/ intra	CHASEDB1	0.7437	0.9700	0.9777	0.7354	0.7751
	STARE	0.5528	0.9586	0.9340	0.6381	0.7127
	DRIVE	<b>0.4493</b>	0.9490	0.9242	0.5542	0.6653
S: w/ intra +inter	CHASEDB1	0.7559	0.9710	0.9795	0.7453	0.7818
	STARE	0.6138	0.9583	0.9361	0.6605	0.7248
	DRIVE	<b>0.4974</b>	0.9557	0.9314	0.6130	0.6980
<b>S: w/ intra + inter + cross</b>	CHASEDB1	<b>0.7804</b>	<b>0.9728</b>	<b>0.9837</b>	<b>0.7637</b>	<b>0.7940</b>
	STARE	<b>0.6252</b>	<b>0.9612</b>	<b>0.9504</b>	<b>0.6803</b>	<b>0.7375</b>
	DRIVE	<b>0.5061</b>	<b>0.9582</b>	<b>0.9490</b>	<b>0.6309</b>	<b>0.7087</b>

the segmentation performance and generalization ability of student are significantly improved. As shown in Table. III, the middle three-row shows that our intra-coupling distillation could provide the generalizable knowledge for student. Concretely, the performance gap is significant decreasing from 0.4028 to 0.2363 on the SE indicator. Meanwhile, performance improves dramatically with all metrics, compared with scratch-trained student in the CHAOS testing phase. Moreover, when intra-coupling distillation is utilized, the student performance on the three retinal vessel segmentation datasets is significantly improved. Qualitatively, We visualize the results of the above ablation experiments as depicted in Fig. 9 and Fig. 10. After adding intra-coupling graph supervision, the student model is more sensitive to details.

2) *Ablation on Inter-coupling Graph Distillation:* To evaluate the influence of our proposed Inter-coupling graph distillation schema, we conduct experiments by accumulating this supervision on the previous versions as reported in Table. III

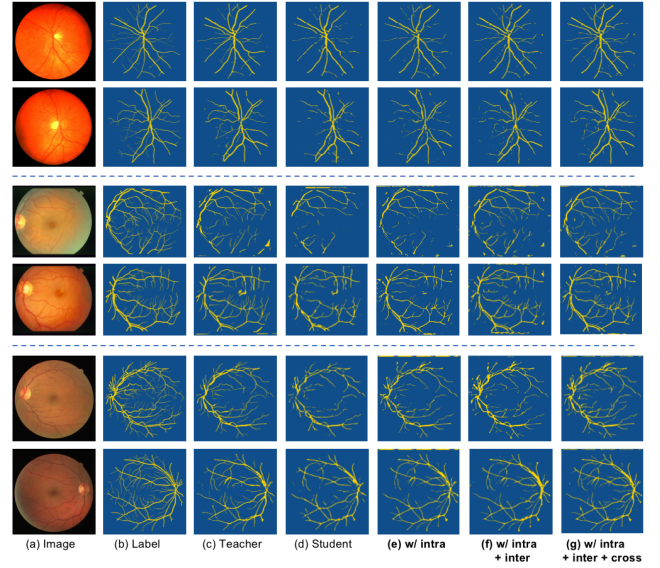


Fig. 10. The visual comparisons of ablation study on the retinal vessel segmentation task. The top two-row samples are from CHASEDB1 dataset, the middle two-row samples are from STARE dataset, and the bottom two-row samples are from the DRIVE dataset. Notably, all the models are trained on the CHASEDB1 dataset and directly tested on three datasets.

TABLE V  
FSD RESULTS ON RETINAL VESSEL AND LIVER SEGMENTATION TASKS.  $\downarrow$  INDICATES THE LOWER, THE BETTER.

Model	Fréchet Semantic Distance (FSD) $\downarrow$				
Dataset	CHASEDB1	STARE	DRIVE	CHAOS	LITS
T: FANet w/ o	53.28	55.94	56.31	79.93	82.29
S: Mobile Unet w/ o	1660.94	2331.28	2790.26	1445.79	1682.39
T: FANet w/ A	34.23	35.40	36.29	45.73	46.84
S: Mobile Unet w/ A	146.85	147.17	148.31	121.52	123.00
<b>S: GKD</b>	<b>55.11</b>	<b>55.51</b>	<b>56.06</b>	<b>45.00</b>	<b>49.37</b>

and Table. IV. As for the SE indicator, the student model achieves the best performance of 0.9474 in the CHAOS testing phase. Meanwhile, the gap between the two liver segmentation datasets is obviously reduced. Specifically, there is a 22% (*i.e.*  $(0.2363 - 0.1842)/0.2363 \approx 22.0\%$ , colored in blue for better view.) decrease compared to only leveraging the intra-coupling graph distillation schema. In the retina vessel segmentation testing phase, all the metrics reach the higher tiers compared with the last model version. In particular, the SE indicator achieves about 10.7% (*i.e.*  $(0.4974 - 0.4493)/0.4493 \approx 10.7\%$ , colored in blue for better view.) improvement on the DRIVE dataset. This indicates the importance of inter-coupling graph distillation on cross-domain medical image segmentation. After adopting inter-coupling graph distillation, the incorrect segmentation of indistinguishable background pixels is greatly suppressed, as could be observed from results under 'w/ intra + inter' in Fig. 9 and Fig. 10.



TABLE VI  
RESULTS ON CHAOS AND LITS DATASETS WITH DIFFERENT STUDENTS.  $\uparrow$  INDICATES THE HIGHER, THE BETTER.  $\downarrow$  INDICATES THE LOWER, THE BETTER.

Model				SE $\uparrow$			ACC $\uparrow$			AUC $\uparrow$			F1 $\uparrow$			mIOU $\uparrow$		
Datasets		FLOPs(G) $\downarrow$	Params(M) $\downarrow$	CHAOS	LITS	GAP $\downarrow$	CHAOS	LITS	GAP $\downarrow$	CHAOS	LITS	GAP $\downarrow$	CHAOS	LITS	GAP $\downarrow$	CHAOS	LITS	GAP $\downarrow$
Teacher	FANet	171.556	38.250	0.9613	0.8356	0.1257	0.9932	0.9835	0.0097	0.9986	0.9908	0.0078	0.9401	0.8647	0.0754	0.9399	0.8721	0.0678
Student	Mobile Unet w/ o	1.492	4.640	0.8840	0.4812	0.4028	0.9899	0.9625	0.0274	0.9972	0.9723	0.0249	0.9057	0.6180	0.2877	0.9085	0.7042	0.2043
	Mobile Unet w/ GKD			<b>0.9451</b>	<b>0.8251</b>	<b>0.1200</b>	<b>0.9924</b>	<b>0.9825</b>	<b>0.0099</b>	<b>0.9984</b>	<b>0.9912</b>	<b>0.0072</b>	<b>0.9320</b>	<b>0.8560</b>	<b>0.0760</b>	<b>0.9323</b>	<b>0.8649</b>	<b>0.0674</b>
	ENet w/ o	0.516	0.349	0.8924	0.6816	0.2108	0.9851	0.9175	0.0136	0.9940	0.9555	0.0385	0.8682	0.7510	0.1172	0.9757	0.7857	0.1900
	ENet w/ GKD			<b>0.9550</b>	<b>0.8326</b>	<b>0.1224</b>	<b>0.9919</b>	<b>0.9807</b>	<b>0.0112</b>	<b>0.9974</b>	<b>0.9811</b>	<b>0.0173</b>	<b>0.9281</b>	<b>0.8445</b>	<b>0.0836</b>	<b>0.9287</b>	<b>0.8552</b>	<b>0.0735</b>

3) *Ablation on Domain-Invariant Cross Distillation:* We add the Domain-Invariant Cross Distillation (DICD) schema as the final component of our proposed GKD framework. In DICD, the model-specific features are cross-reconstructed by exchanging the decoding headers of MSAN. The features reconstructed from regularized domain-invariant vectors contain more pure semantic information intuitively, as shown in Fig. 4. Such semantic information facilitates the generalization of the student model in cross-domain scenes. We leverage the powerful pre-trained teacher model to provide the supervision of the encoder and decoder of student jointly. Thus, after adding the DICD, the whole performance of the student model is further improved. Segmented results obtained by different variants of the proposed model are shown in Fig. 9 and Fig. 10. It could be observed that the pixel prediction results of the semantic foreground are gradually optimized via a scratch-trained model. Although in the final version the SE metric on the CHAOS dataset slight declined, the GKD achieves the best results in most metrics as reported in Table. III and Table. IV.

#### F. Domain-invariant Verification of GKD

To further verify the domain-invariant representative ability of our proposed MSAN, we introduce a new quantitative metric named Fréchet Semantic Distance (FSD). The FSD is computed by the Fréchet Distance between the latent vectors from SAN (or TAN) and P-SAE. In ACT, the main step is to provide the domain-invariant regularization (the word ‘Alignment’ in Fig. 4) for the TAN and SAN. This could restrict the latent vectors from these two models to align in the consistent semantic space, leading to domain-invariant representations. Thus, we conduct the comparative experiments on the above mentioned 5 datasets. As reported in Table. V, ‘w/ o’ denotes dropping the alignment step when training the MSAN; ‘w/ A’ denotes adopting the alignment step. After the alignment operation, the FSD of scratch-trained student model is dramatically decreased, which means the domain-specific features are mapped to be more domain-invariant. This also indicates the latent vectors embedded from SAN are more consistent with vectors embedded by TAN. Furthermore, after conducting the DCGD and DICD schemes, our GKD achieves much lower FSD than the scratch-trained student model with the ‘w/ A’ operation (*i.e.* 1660.94  $\rightarrow$  146.85  $\rightarrow$  55.11 in CHASEDB1 dataset). This proves that our proposed GKD could further facilitate better domain-invariant representations progressively. As for the direct testing datasets (*i.e.* STARE,

DRIVE, and LITS), the FSD of the student model is also significantly decreased after conducting our proposed GKD.

#### G. Generalization on Different Students

To further evaluate the generalization of our proposed GKD with different shallow network architectures, we adopt the lightweight ENet [49] as an additional student. The comparison results are reported in Table. VI, all the hyper-parameters are consistent with previous experiments. We observed that for both Mobile Unet based and ENet based student, they all have much lower FLOPs and Params than the complicated teacher model. These shallow network architectures result in poor performance on the CHAOS and LITS datasets. However, after the distillation by GKD, both the lightweight student models obtain significant improvements on all metrics.

### V. CONCLUSION

In this paper, we propose a generalizable knowledge distillation framework for efficient medical image segmentation, namely GKD. In GKD, we take full advantage of a Pre-trained Semantic Autoencoder (P-SAE) to provide the domain-invariant regularization for training the Model-Specific Alignment Networks (MSAN). Guided by MSAN, two generalizable knowledge distillation schemes named Dual Contrastive Graph Distillation (DCGD) and Domain-Invariant Cross Distillation (DICD) are proposed to improve the performance of lightweight models in cross-domain scenes. Moreover, we introduce a new metric named Fréchet Semantic Distance (FSD) to verify the effectiveness of the regularized domain-invariant features. As a result, our method achieves outstanding performance compared with various knowledge distillation counterparts on liver and retinal vessel segmentation tasks. In the future, we would like to investigate the knowledge distillation approaches for cross-modality medical image analysis.

### REFERENCES

- [1] O. Ronneberger, P. Fischer, and T. Brox, “U-net: Convolutional networks for biomedical image segmentation,” in *Proc. Int. Conf. Med. Image Comput. Comput. Assist. Intervent. (MICCAI)*, 2015, pp. 234–241.
- [2] Z. Zhou, M. M. R. Siddiquee, N. Tajbakhsh, and J. Liang, “UNet++: Redesigning skip connections to exploit multiscale features in image segmentation,” *IEEE Trans. Med. Imag. (TMI)*, vol. 39, no. 6, pp. 1856–1867, 2019.
- [3] F. Milletari, N. Navab, and S. A. Ahmadi, “V-net: Fully convolutional neural networks for volumetric medical image segmentation,” in *Proc. Fourth Int. Conf. 3D Vis. (3DV)*, Oct. 2016, pp. 565–571.



- [4] Y. Jiang, X. Gu, D. Wu, et al., "A Novel Negative-Transfer-Resistant Fuzzy Clustering Model With a Shared Cross-Domain Transfer Latent Space and its Application to Brain CT Image Segmentation," *IEEE/ACM Trans. Comput. Biol. Bioinf.*, vol. 18, no. 1, pp. 40-52, Feb. 2021.
- [5] X. Liu, F. Xing, C. Yang, et al., "Adapting off-the-shelf source segmenter for target medical image segmentation," in *Proc. Int. Conf. Med. Image Comput. Comput. Assist. Intervent. (MICCAI)*, Sept. 2021, pp. 549-559.
- [6] D. Zou, Q. Zhu, and P. Yan, "Unsupervised domain adaptation with dualscheme fusion network for medical image segmentation," in *Proc. 29th Int. Joint Conf. Artif. Intell. (IJCAI)*, 2020, pp. 3291-3298.
- [7] X. Han et al., "Deep Symmetric Adaptation Network for Cross-Modality Medical Image Segmentation," *IEEE Trans. Med. Imag. (TMI)*, vol. 41, no. 1, pp. 121-132, Jan. 2022.
- [8] X. Han, L. Qi, Q. Yu, et al., "Anatomy-Regularized Representation Learning for Cross-Modality Medical Image Segmentation," *IEEE Trans. Med. Imag. (TMI)*, vol. 40, no. 1, pp. 274-285, Jan. 2021.
- [9] L. Zhang, X. Wang, D. Yang, et al., "Generalizing Deep Learning for Medical Image Segmentation to Unseen Domains via Deep Stacked Transformation," *IEEE Trans. Med. Imag. (TMI)*, vol. 39, no. 7, pp. 2531-2540, Jul. 2020.
- [10] M. Perslev, E. B. Dam, A. Pai, et al., "One network to segment them all: A general, lightweight system for accurate 3d medical image segmentation," in *Proc. Int. Conf. Med. Image Comput. Comput. Assist. Intervent. (MICCAI)* Oct. 2019, pp. 30-38.
- [11] D. Qin, J. J. Bu, Z. Liu, et al., "Efficient Medical Image Segmentation Based on Knowledge Distillation," *IEEE Trans. Med. Imag. (TMI)*, vol. 40, no. 12, pp. 3820-3831, Dec. 2021.
- [12] A. G. Howard, M. Zhu, B. Chen, et al., "Mobilenets: Efficient convolutional neural networks for mobile vision applications," 2017, *arXiv:1704.04861*. [Online]. Available: <https://arxiv.org/abs/1704.04861>.
- [13] J. Hu, L. Shen, and G. Sun, "Squeeze-and-excitation networks," in *Proc. IEEE/CVF Conf. Comput. Vis. Pattern Recognit. (CVPR)*, Jun. 2018, pp. 7132-7141.
- [14] X. Li, W. Wang, X. Hu, et al., "Selective kernel networks," in *Proc. IEEE/CVF Conf. Comput. Vis. Pattern Recognit. (CVPR)*, Jun. 2019, pp. 510-519.
- [15] Y. He, P. Liu, Z. Wang, et al., "Filter pruning via geometric median for deep convolutional neural networks acceleration," in *Proc. IEEE/CVF Conf. Comput. Vis. Pattern Recognit. (CVPR)*, Jun. 2019, pp. 4340-4349.
- [16] Y. He, G. Kang, X. Dong, et al., "Soft filter pruning for accelerating deep convolutional neural networks," in *Proc. 27th Int. Joint Conf. Artif. Intell. (IJCAI)*, Jul. 2018, pp. 2234-2240.
- [17] Z. Wang, C. Li, and X. Wang, "Convolutional neural network pruning with structural redundancy reduction," in *Proc. IEEE/CVF Conf. Comput. Vis. Pattern Recognit. (CVPR)*, Jun. 2021, pp. 14913-14922.
- [18] G. Hinton, O. Vinyals, and J. Dean, "Distilling the knowledge in a neural network," 2015, *arXiv:1503.02531*. [Online]. Available: <https://arxiv.org/abs/1503.02531>.
- [19] S. Zagoruyko, and N. Komodakis, "Paying more attention to attention: improving the performance of convolutional neural networks via attention transfer," in *Proc. Int. Conf. Learn. Represent. (ICLR)*, Jun. 2017, pp. 1-13.
- [20] J. Yim, D. Joo, J. Bae, et al., "A gift from knowledge distillation: Fast optimization, network minimization and transfer learning," in *Proc. IEEE Conf. Comput. Vis. Pattern Recognit. (CVPR)*, Jul. 2017, pp. 4133-4141.
- [21] Y. Liu, C. Shu, J. Wang, et al., "Structured knowledge distillation for dense prediction," *IEEE Trans. Pattern Anal. Mach. Intell. (TPAMI)*, Jun. 2020.
- [22] Y. Wang, W. Zhou, T. Jiang, et al., "Intra-class feature variation distillation for semantic segmentation," in *Proc. Euro. Conf. Comput. Vis. (ECCV)*, Nov. 2020, pp. 346-362.
- [23] W. Zou, X. Qi, Z. Wu, et al., "CoCo distillnet: a cross-layer correlation distillation network for pathological gastric cancer segmentation," in *Proc. IEEE Int. Conf. Bioinform. Biomed. (BIBM)*, Dec. 2021, pp. 1227-1234.
- [24] C. You, Y. Zhou, R. Zhao, et al., "SimCVD: Simple Contrastive Voxel-Wise Representation Distillation for Semi-Supervised Medical Image Segmentation," *IEEE Trans. Med. Imag. (TMI)*, Mar. 2022.
- [25] Y. Zhou, H. Chen, H. Lin, et al., "Deep semi-supervised knowledge distillation for overlapping cervical cell instance segmentation," in *Proc. Int. Conf. Med. Image Comput. Comput. Assist. Intervent. (MICCAI)*, Oct. 2020, pp. 521-531.
- [26] R. Aljundi, and T. Tuytelaars, "Lightweight unsupervised domain adaptation by convolutional filter reconstruction," in *Proc. Eur. Conf. Comput. Vis. (ECCV)*, Oct. 2016, pp. 508-515.
- [27] S. Ye, et al., "Light-weight calibrator: a separable component for unsupervised domain adaptation," in *Proc. IEEE/CVF Conf. Comput. Vis. Pattern Recognit. (CVPR)*, 2020, pp. 13736-13745.
- [28] S. Li, M. Xie, K. Gong, et al., "Transferable semantic augmentation for domain adaptation," in *Proc. IEEE/CVF Conf. Comput. Vis. Pattern Recognit. (CVPR)*, Jun. 2021, pp. 11516-11525.
- [29] T. Chen, S. Kornblith, M. Norouzi, et al., "A simple framework for contrastive learning of visual representations," in *Proc. Int. Conf. Mach. Learn. (ICML)*, Nov. 2020, pp. 1597-1607.
- [30] A. V. D. Oord, Y. Li, and O. Vinyals, "Representation learning with contrastive predictive coding," 2018, *arXiv:1807.03748*. [Online]. Available: <https://arxiv.org/abs/1807.03748>.
- [31] K. He, H. Fan, Y. Wu, et al., "Momentum contrast for unsupervised visual representation learning," in *Proc. IEEE/CVF Conf. Comput. Vis. Pattern Recognit. (CVPR)*, Jun. 2020, pp. 9729-9738.
- [32] Y. Tian, D. Krishnan, and P. Isola, "Contrastive Representation Distillation," in *Proc. Int. Conf. Learn. Represent. (ICLR)*, Sep. 2019.
- [33] L. Wang, J. Huang, Y. Li, et al., "Improving weakly supervised visual grounding by contrastive knowledge distillation," in *Proc. IEEE/CVF Conf. Comput. Vis. Pattern Recognit. (CVPR)*, Jun. 2021, pp. 14090-14100.
- [34] J. M. J. Valanarasu, V. A. Sindagi, I. Hacihaliloglu, et al., "Kiu-net: Towards accurate segmentation of biomedical images using over-complete representations," in *Proc. Int. Conf. Med. Image Comput. Comput. Assist. Intervent. (MICCAI)*, Oct. 2020, pp. 363-373.
- [35] K. Li, X. Qi, Y. Luo, et al., "Accurate Retinal Vessel Segmentation in Color Fundus Images via Fully Attention-Based Networks," *IEEE J. Biomed. Health Inform. (JBHI)*, vol. 25, no. 6, pp. 2071-2081, Jun. 2021.
- [36] S. Takahama, Y. Kurose, Y. Mukuta, et al., "Multi-stage pathological image classification using semantic segmentation," in *Proc. IEEE Int. Conf. Comput. Vis. (ICCV)*, Oct. 2019, pp. 10702-10711.
- [37] X. Wang, T. Xiang, C. Zhang, et al., "Bix-nas: Searching efficient bi-directional architecture for medical image segmentation," in *Proc. Int. Conf. Med. Image Comput. Comput. Assist. Intervent. (MICCAI)*, Sep. 2021, pp. 229-238.
- [38] E. Creager, J. H. Jacobsen, and R. Zemel, "Environment inference for invariant learning," in *Proc. Int. Conf. Mach. Learn. (ICML)*, Jul. 2021, pp. 2189-2200.
- [39] J. Li, W. Liu, Y. Zhou, J. Yu, D. Tao, and C. Xu, "Domain-invariant Graph for Adaptive Semi-supervised Domain Adaptation," *ACM Trans. Multimedia Comput. Commun. Appl. (TOMM)*, vol. 18, no. 3, pp. 1-18, 2022.
- [40] A. E. Kavur, N. S. Gezer, M. Barış, et al., "CHAOS challenge-combined (CT-MR) healthy abdominal organ segmentation," *Med. Image Anal.*, vol. 69, 2021.
- [41] P. Bilic, P. F. Christ, E. Vorontsov, et al., "The liver tumor segmentation benchmark (lits)," 2019, *arXiv:1901.04056*. [Online]. Available: <https://arxiv.org/abs/1901.04056>.
- [42] J. Staaf, M. D. Abramoff, M. Niemeijer, M. A. Viergever, and B. Van Ginneken, "Ridge-based vessel segmentation in color images of the retina," *IEEE Trans. Med. Imag. (TMI)*, vol. 23, no. 4, pp. 501-509, 2004.
- [43] A. D. Hoover, V. Kouznetsova, and M. Goldbaum, "Locating blood vessels in retinal images by piecewise threshold probing of a matched filter response," *IEEE Trans. Med. Imag. (TMI)*, vol. 19, no. 3, pp. 203-210, Mar. 2000.
- [44] M. M. Fraz, P. Remagnino, A. Hoppe, et al., "An ensemble classification-based approach applied to retinal blood vessel segmentation," *IEEE Trans. Biomed. Eng. (TBE)*, vol. 59, no. 9, pp. 2538-2548, Sep. 2012.
- [45] T. Fawcett, "An introduction to ROC analysis," *Pattern. Recognit. Lett.*, vol. 27, no. 8, pp. 861-874, 2006.
- [46] M. Lucic, K. Kurach, M. Michalski, S. Gelly, and O. Bousquet, "Are GANs created equal? A large-scale study," 2017, *arXiv:1706.08500*, [Online]. Available: <https://arxiv.org/abs/1711.10337>.
- [47] C. Szegedy, V. Vanhoucke, S. Ioffe, J. Shlens, and Z. Wojna, "Rethinking the inception architecture for computer vision," in *Proc. IEEE/CVF Conf. Comput. Vis. Pattern Recognit. (CVPR)*, June. 2016, pp. 2818-2826.
- [48] M. Sandler, A. Howard, M. Zhu, A. Zhmoginov, and L. C. Chen, "Mobilenetv2: Inverted residuals and linear bottlenecks," in *Proc. IEEE/CVF Conf. Comput. Vis. Pattern Recognit. (CVPR)*, Jun. 2018, pp. 4510-4520.
- [49] A. Paszke, A. Chaurasia, S. Kim, and E. Culurciello, "Enet: A deep neural network architecture for real-time semantic segmentation," 2016, *arXiv: 1606.02147*, [Online]. Available: <https://arxiv.org/abs/1606.02147>.
- [50] A. Paszke, S. Gross, F. Massa, et al., "PyTorch: An imperative style, high-performance deep learning library," in *Proc. Adv. Neural Inf. Process. Syst.*, 2019, pp. 8026-8037.
- [51] J. N. Kundu, S. Seth, A. Jamkhandi, et al., "Non-local latent relation distillation for self-adaptive 3D human pose estimation," *Advances in Neural Information Processing Systems*, in *Proc. Adv. Neural Inf. Process. Syst. (NIPS)*, 2021, pp. 158-171.